

Air Force Institute of Technology

AFIT Scholar

Faculty Publications

8-8-2016

Estimating Index of Refraction from Polarimetric Hyperspectral Imaging Measurements

Jacob A. Martin

Air Force Research Laboratory

Kevin C. Gross

Air Force Institute of Technology

Follow this and additional works at: <https://scholar.afit.edu/facpub>



Part of the [Optics Commons](#), and the [Signal Processing Commons](#)

Recommended Citation

Jacob A. Martin and Kevin C. Gross, "Estimating index of refraction from polarimetric hyperspectral imaging measurements," *Opt. Express* 24, 17928-17940 (2016). <https://doi.org/10.1364/OE.24.017928>

This Article is brought to you for free and open access by AFIT Scholar. It has been accepted for inclusion in Faculty Publications by an authorized administrator of AFIT Scholar. For more information, please contact richard.mansfield@afit.edu.

Estimating index of refraction from polarimetric hyperspectral imaging measurements

JACOB A. MARTIN^{1,2} AND KEVIN C. GROSS^{2,*}

¹Air Force Research Laboratories, RYMT, Wright-Patterson AFB, OH 45433, USA

²Air Force Institute of Technology, 2950 Hobson Way, Wright-Patterson AFB, OH 45433, USA

*kevin.gross@afit.edu

Abstract: Current material identification techniques rely on estimating reflectivity or emissivity which vary with viewing angle. As off-nadir remote sensing platforms become increasingly prevalent, techniques robust to changing viewing geometries are desired. A technique leveraging polarimetric hyperspectral imaging (P-HSI), to estimate complex index of refraction, $\hat{N}(\tilde{\nu})$, an inherent material property, is presented. The imaginary component of $\hat{N}(\tilde{\nu})$ is modeled using a small number of “knot” points and interpolation at in-between frequencies $\tilde{\nu}$. The real component is derived via the Kramers-Kronig relationship. P-HSI measurements of blackbody radiation scattered off of a smooth quartz window show that $\hat{N}(\tilde{\nu})$ can be retrieved to within 0.08 RMS error between $875\text{ cm}^{-1} \leq \tilde{\nu} \leq 1250\text{ cm}^{-1}$. P-HSI emission measurements of a heated smooth Pyrex beaker also enable successful $\hat{N}(\tilde{\nu})$ estimates, which are also invariant to object temperature.

OCIS codes: (010.0280) Remote sensing and sensors; (100.2000) Digital image processing; (110.4234) Multispectral and hyperspectral imaging; (110.6820) Thermal imaging; (120.2130) Ellipsometry and polarimetry.

References and links

1. M. T. Eismann, *Hyperspectral Remote Sensing* (SPIE, 2012).
2. A. B. Kahle, D. P. Madura, and J. M. Soha, “Middle infrared multispectral aircraft scanner data: analysis for geological applications,” *Appl. Opt.* **19**, 2279–2290 (1980).
3. P. S. Kealy and S. J. Hook, “Separating temperature and emissivity in thermal infrared multispectral scanner data: Implications for recovering land surface temperatures,” *IEEE Trans. Geosci. Remote Sensing* **31**, 1155–1164 (1993).
4. K. Watson, “Two-temperature method for measuring emissivity,” *Remote Sensing of Environment* **42**, 117–121 (1992).
5. Z. Wan and J. Dozier, “A generalized split-window algorithm for retrieving land-surface temperature from space,” *IEEE Trans. Geosci. Remote Sensing* **34**, 892–905 (1996).
6. J. Cheng, Q. Xiao, X. Li, and Q. Liu, “Multi-layer perceptron neural network based algorithm for simultaneous retrieving temperature and emissivity from hyperspectral FTIR dataset,” in *Proceedings of IEEE International Geoscience and Remote Sensing Symposium (IEEE, 2007)*, pp. 4383–4385.
7. J. Cheng, Q. Liu, X. Li, Q. Xiao, Q. Liu, and Y. Du, “Correlation-based temperature and emissivity separation algorithm,” *Science in China Series D: Earth Sciences* **51**, 357–369 (2008).
8. J. Cheng, S. Liang, J. Wang, and X. Li, “A stepwise refining algorithm of temperature and emissivity separation for hyperspectral thermal infrared data,” *IEEE Transactions on Geoscience and Remote Sensing* **48**, 1588–1597 (2010).
9. C. C. Borel and R. F. Tuttle, “Recent advances in temperature-emissivity separation algorithms,” in *Proceedings of IEEE Aerospace Conference*, pp. 1–14, March 2011.
10. J. Dozier and S. G. Warren, “Effect of viewing angle on the infrared brightness temperature of snow,” *Water Resources Research* **18**, 1424–1434 (1982).
11. J. Labed and M. P. Stoll, “Angular variation of land surface spectral emissivity in the thermal infrared: laboratory investigations of bare soils,” *Int. J. Remote Sensing* **12**, 2299–2310 (1991).
12. J. P. Lagouarde, Y. H. Kerr, and Y. Brunet, “An experimental study of angular effects on surface temperature for various plant canopies and bare soils,” *Agricultural and Forest Meteorology* **77**, 167–190 (1995).
13. J. A. Sobrino and J. Cuenca, “Angular variation of thermal infrared emissivity for some natural surfaces from experimental measurements,” *Appl. Opt.* **38**, 3931–3936 (1999).
14. C. J. Deloye, M. S. West, and J. M. Grossmann, “Changes in apparent emissivity as a function of viewing geometry,” *Proc. SPIE* **8040**, 80400J (2011).
15. L. B. Wolff, “Polarization-based material classification from specular reflection,” *IEEE Trans. Pattern Analysis and Machine Intelligence* **12**, 1059–1071 (1990).
16. L. B. Wolff and T. E. Boulton, “Constraining object features using a polarization reflectance model,” *IEEE Trans. Pattern Analysis and Machine Intelligence* **13**, 635–657 (1991).
17. V. Thilak, C. D. Creusere, and D. G. Voelz, “Estimating the complex index of refraction and view angle of an object using multiple polarization measurements,” in *Proceedings of IEEE Fourtieth Asilomar Conference on Signal,*

- Systems, and Computers (IEEE, 2006), pp. 1067–1071.
18. V. Thilak, C. D. Creusere, and D. G. Voelz, “Material classification using passive polarimetric imagery,” in Proceedings of IEEE International Conference of Image Processing IV (IEEE, 2007), pp. 121–124.
 19. V. Thilak, D. G. Voelz, and C. D. Creusere, “Polarization-based index of refraction and reflection angle estimation for remote sensing applications,” *Appl. Opt.* **46**, 7527–7536 (2007).
 20. V. Thilak, C. D. Creusere, and D. G. Voelz, “Passive polarimetric imagery based material classification for remote sensing applications,” in Proceedings of IEEE Southwest Symposium on Image Analysis and Interpretation (IEEE, 2008), pp. 153–156.
 21. V. Thilak, C. D. Creusere, and D. G. Voelz, “Passive polarimetric imagery-based material classification robust to illumination source position and viewpoint,” *IEEE Trans. Image Processing* **20**, 288–292 (2011).
 22. C. P. Huynh, A. Robles-Kelly, and E. Hancock, “Shape and refractive index recovery from single-view polarisation images,” in IEEE Conference on Computer Vision and Pattern Recognition, pp. 1229–1236, 2010.
 23. M. P. Fetrow, D. L. Wellems, S. H. Sposato, K. P. Bishop, T. R. Caudill, M. L. Davis, and E. R. Simrell, “Results of a new polarization simulation,” *Proc. SPIE* **4481**, 149–162 (2002).
 24. J. D. Jackson, *Classical Electrodynamics*, 3rd Ed. (John Wiley And Sons, 1999).
 25. D. A. LeMaster and M. T. Eismann, *Passive Polarimetric Imaging, in Multi-Dimensional Imaging* (John Wiley And Sons, 2014).
 26. J. R. Schott, *Fundamentals of Polarimetric Remote Sensing* (SPIE, 2009).
 27. D. L. Jordan and G. Lewis, “Measurements of the effect of surface roughness on the polarization state of thermally emitted radiation,” *Opt. Lett.* **19**, 692–694 (1994).
 28. R. G. Priest and T. A. Germer, “Polarimetric BRDF in the Microfacet Model: Theory and Measurements,” Naval Research Lab (2000).
 29. R. G. Priest and S. R. Meier, “Polarimetric microfacet scattering theory with applications to absorptive and reflective surfaces,” *Opt. Eng.* **41**, 988–993 (2002).
 30. C. An and K. Zeringue, “Scattering and Emission Polarization Simulation for Simple Objects,” *Proc. SPIE* **5432**, 543492 (2004).
 31. I. B. A.R. Forouhi, “Optical dispersion relations for amorphous semiconductors and amorphous dielectrics,” *Phys. Rev. B* **34**, 7018–7026 (1986).
 32. R. Brendel and D. Bormann, “An infrared dielectric function model for amorphous solids,” *J. Appl. Phys.* **71** (1992).
 33. J. Humlicek, *Handbook of Ellipsometry* (William Andrew Publishing, 2005).
 34. MATLAB Release 2015b, The MathWorks, Inc., Natick, Massachusetts, United States.
 35. J.L. Musfeldt and D.B. Tanner and A.J. Paine, “Method for determination of optical properties of highly conjugated pigments,” *J. Opt. Soc. Am. A* **10**, 2648–7026 (1993).
 36. J. G. Holder, “Polarimetric calibration and characterization of the Telops field portable polarimetric-hyperspectral imager,” Master’s thesis, Air Force Institute of Technology, March 2014.
 37. H. Revercomb, H. Bujis, H. Howell, D. LaPorte, W. Smith, and L. Sromovsky, “Radiometric calibration of IR Fourier transform spectrometers: solution to a problem with the high-resolution interferometer sounder,” *Appl. Opt.* **27**, 3210–3218 (1988).
 38. K. P. Gurton and R. Dahmani, “Effect of surface roughness and complex indices of refraction on polarized thermal emission,” *Appl. Opt.* **44**, 5361–5367 (2005).

1. Introduction

Many material classification and identification methods have been developed using hyperspectral imagery, see [1] for a good overview. These technique generally fall into one of two categories: the first uses the calibrated radiance measurements to classify and identify materials, the other interprets the radiance measurements to estimate either an emissivity or reflectivity spectra for each pixel and uses this signature to classify and identify materials. In the radiance domain, the same target can produce different signatures based on changes in object temperature, viewing geometry, atmospheric conditions, etc. Because of this, a single target signature often cannot be effectively used to identify the material. Instead, a group of target signatures, commonly referred to as a subspace is used to classify a material. A problem arises, however, when dealing with spectrally similar materials because these subspaces can “overlap” making classification difficult. When working in the long-wave infrared (LWIR), emissivity is often the estimated quantity for material identification. This type of problem is commonly known as temperature-emissivity separation (TES) because it is necessary to determine both the temperature and spectral emissivity of a material to fully describe its emitted radiance. This is typically an underdetermined problem because, in addition to the unknown emissivity values in each spectral band, the temperature is

also unknown. Several TES algorithms exist in the literature — see [2–9] for a few — and they typically make some simplifying assumptions or introduce *a priori* information to reduce the effective number of variables. A problem arises when the sensor location is changing relative to the target because emissivity varies with viewing angle. [10–14] To properly account for this, it again becomes necessary to use an ensemble of spectra, this time based on changes in emissivity, to describe a material instead of a single spectrum. Estimating the complex index of refraction may be advantageous for material identification because, in a vast majority of operational scenarios, it is invariant to viewing geometry — birefringent materials and metamaterials being potential exceptions — and insensitive to object temperature over typical terrestrial variations.

While extensive work has been done using hyperspectral imagery for material classification and identification, less work has been done using polarimetry, and very little has focused on exploiting simultaneous hyperspectral and polarimetric imaging measurements. Early work by Wolff [15, 16] used polarization to distinguishing metals from dielectric materials. The approach leveraged the fact that dielectric surfaces tend to polarize light much more strongly than metal surfaces. While this is useful in some situations, more information about the material being observed is often required. Additionally, dielectric materials can also have small polarization signatures, especially when viewed near-normal, causing them to be misclassified as metals. Thilak *et al.* explored using polarization to simultaneously estimate both index of refraction and surface normal angle [17–21]. Their method first estimated the index of refraction from degree of linear polarization (DoLP) measurements, then used this effective index of refraction to calculate the surface normal angle. This work used only a single wavelength, however, limiting its utility for material identification. Additionally, since only DoLP was used to estimate index of refraction, identifying materials with small polarization was difficult.

Huynh *et al.* used multispectral imagery to extract both surface normal and index of refraction [22]. By fitting a sinusoid to the intensity measured at several angles, the index of refraction was estimated from the sinusoid's extrema and extracted angle of polarization. The spectral dependence of the index was modeled using the Cauchy dispersion equation. While this approach does not account for the imaginary component of the refractive index, the idea of modeling its spectral variation to reduce the number of parameters by imposing physics-based constraints is emulated in this work. Fetrow *et al.* applied a method for retrieving index of refraction to LWIR hyperspectral polarimetric measurements [23]. Their method assumed *a priori* knowledge of downwelling radiance and surface temperature. They tested their model using a hemispherical dome to control the radiance being reflected off the target. Careful measurements of the dome and sample surface temperatures were taken. Glass plates were measured at 12 different angles relative to the sensor ranging from normal to 80° . To solve for index of refraction, they used a fitting algorithm to minimize the sum of squared errors from both the polarized and unpolarized radiance measurements, an approach also used in this work. In order to arrive at a realistic value for all wavelengths, the constraints on the fit had to be loosened, which led to fit uncertainty exceeding ± 1 for both the real and imaginary components at some wavelengths.

The goal of this work is to leverage the spectral variation of emitted and scattered polarized radiation from an object to estimate its complex index of refraction, \hat{N} , in a way that is both accurate and invariant to scene conditions. In order to do this, a fitting routine is developed using polarimetric hyperspectral imaging (P-HSI) measurements to determine \hat{N} and surface temperature. The scope of the present work is to establish the methodology and experimentally demonstrate \hat{N} retrievals under carefully-controlled laboratory conditions for smooth — relative to the wavelength of light — surfaces. Additional levels of complexity such as dealing with surface roughness, atmospheric compensation, and mixed pixels are the subject of on-going work.

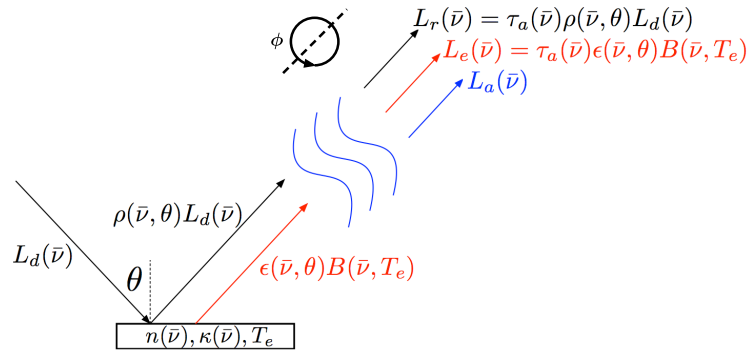


Fig. 1. Basic schematic of the sources of radiance arriving at the sensor.

2. Theory

Assuming a smooth (relative to the wavelengths observed), planar surface comprised of a homogeneous material, the index of refraction can be used to determine its reflectance, ρ_s and ρ_p , via Fresnel's equations [24]:

$$\begin{aligned}\rho_s(\tilde{\nu}) &= \left| \frac{\hat{N}(\tilde{\nu}) \cos \theta_i - \sqrt{1 - \hat{N}(\tilde{\nu})^2 \sin^2 \theta_i}}{\hat{N}(\tilde{\nu}) \cos \theta_i + \sqrt{1 - \hat{N}(\tilde{\nu})^2 \sin^2 \theta_i}} \right|^2 \\ \rho_p(\tilde{\nu}) &= \left| \frac{\cos \theta_i - \hat{N}(\tilde{\nu}) \sqrt{1 - \hat{N}(\tilde{\nu})^2 \sin^2 \theta_i}}{\cos \theta_i + \hat{N}(\tilde{\nu}) \sqrt{1 - \hat{N}(\tilde{\nu})^2 \sin^2 \theta_i}} \right|^2.\end{aligned}\quad (1)$$

In the LWIR, the measured radiance comes from three primary sources: the downwelling radiance $L_d(\tilde{\nu})$ reflected by the target $L_r(\tilde{\nu})$, radiance emitted by the target $L_e(\tilde{\nu})$, which is attenuated by atmospheric transmittance $\tau_a(\tilde{\nu})$, and radiance emitted by the atmosphere along the line-of-sight $L_a(\tilde{\nu})$. A basic schematic of this is shown in Fig. 1. The total radiance in each polarization state arriving at the sensor can be expressed as:

$$L_{s,p}(\tilde{\nu}) = \frac{1}{2} \tau_a(\tilde{\nu}) \left[\rho_{s,p}(\tilde{\nu}) L_d(\tilde{\nu}) + \epsilon_{s,p}(\tilde{\nu}) B(\tilde{\nu}, T_e) \right] + L_a(\tilde{\nu}). \quad (2)$$

Here, ϵ_s and ϵ_p denote the polarized emissivities, and $B(\tilde{\nu}, T_e) = 2hc^2\tilde{\nu}^3 [e^{hc\tilde{\nu}/(k_B T_e)} - 1]^{-1}$ represents the spectral radiance of an ideal blackbody, given by the Planckian distribution, at the temperature of the material's surface, T_e . Assuming an opaque material, $\epsilon_{s,p} = 1 - \rho_{s,p}$. Since this work is done in the long-wave infrared (LWIR), downwelling radiance (L_d), atmospheric transmittance (τ), and path radiance (L_a) are all presumed to be unpolarized [25].

From the polarized radiance, the first three elements of the Stokes vector can be expressed as:

$$\begin{aligned}S_0(\tilde{\nu}) &= \tau_a(\tilde{\nu}) \cdot \left[\frac{1}{2} (\rho_s(\tilde{\nu}) + \rho_p(\tilde{\nu})) \cdot (L_d(\tilde{\nu}) - B(\tilde{\nu}, T_e)) + B(\tilde{\nu}, T_e) \right] + L_a(\tilde{\nu}) \\ S_1(\tilde{\nu}) &= \tau_a(\tilde{\nu}) \cdot \frac{1}{2} (\rho_p(\tilde{\nu}) - \rho_s(\tilde{\nu})) \cdot (L_d(\tilde{\nu}) - B(\tilde{\nu}, T_e)) \cdot \cos(2\phi) \\ S_2(\tilde{\nu}) &= \tau_a(\tilde{\nu}) \cdot \frac{1}{2} (\rho_p(\tilde{\nu}) - \rho_s(\tilde{\nu})) \cdot (L_d(\tilde{\nu}) - B(\tilde{\nu}, T_e)) \cdot \sin(2\phi).\end{aligned}\quad (3)$$

Here, ϕ represents the azimuthal angle of rotation about the optical axis of the sensor relative to the plane of reflectance. The fourth Stokes element, $S_3(\tilde{\nu})$, is ignored as circular polarization is negligible for most targets of interest in remote sensing applications [26], and measuring

this term would require additional polarizing elements not currently available in our P-HSI system. In general, this is an underdetermined problem, but modeling the spectral variation in index of refraction reduces the number of required parameters, potentially making this problem overdetermined. It is important to note that while there are three measured quantities (S_0 , S_1 , and S_2) at each spectral point, these do not represent three independent measurements because of the correlation between S_1 and S_2 shown in Eq. (3).

In this work, measurements were collected in a laboratory over a relatively short path length, and a wide-area blackbody was used as the source of downwelling radiation. Thus, it is assumed that $\tau_a(\tilde{\nu}) = 1$, $L_a(\tilde{\nu}) = 0$, and $L_d(\tilde{\nu}) = B(\tilde{\nu}, T_d)$ is Planck's distribution corresponding to temperature T_d . This simplifies Eq. (3) to:

$$\begin{aligned} S_0(\tilde{\nu}) &= \frac{1}{2} (\rho_s(\tilde{\nu}) + \rho_p(\tilde{\nu})) \cdot (B(\tilde{\nu}, T_d) - B(\tilde{\nu}, T_e)) + B(\tilde{\nu}, T_e) \\ S_1(\tilde{\nu}) &= \frac{1}{2} (\rho_p(\tilde{\nu}) - \rho_s(\tilde{\nu})) \cdot (B(\tilde{\nu}, T_d) - B(\tilde{\nu}, T_e)) \cdot \cos(2\phi) \\ S_2(\tilde{\nu}) &= \frac{1}{2} (\rho_p(\tilde{\nu}) - \rho_s(\tilde{\nu})) \cdot (B(\tilde{\nu}, T_d) - B(\tilde{\nu}, T_e)) \cdot \sin(2\phi). \end{aligned} \quad (4)$$

In general, knowing the reflectance is necessary but not sufficient to accurately model the radiance emitted by a target. Surface roughness also affects radiation scattered and emitted by a target. To appreciate the impact of surface roughness on polarized emission in the LWIR, see Jordan and Lewis's work [27]. For example, in that experimental effort, the degree of linear polarization emitted at $10.6 \mu\text{m}$ by warm soda-lime glass at $\theta_i = 80^\circ$ was seen to vary with rms surface roughness (σ) from approximately 55% when $\sigma = 0.02 \mu\text{m}$ to about 23% when $\sigma = 9.89 \mu\text{m}$. Note that while Eqs. (1)–(4) are only valid for a smooth, planar surface of linear dimension many times larger than the wavelength of scattered / emitted light, rough surfaces can often be approximated by a number of randomly oriented smooth surfaces, *i.e.* microfacets, each of which is treated as an ideal Fresnel surface. Numerous polarimetric bidirectional reflectance distribution functions (pBRDF) exist in the literature [28–30]. While smooth surfaces are the focus of this initial effort, surface roughness effects will be incorporated in follow-on work using parametric pBRDFs.

3. Solving for index of refraction

Using the forward model for the spectrally-resolved Stokes vector, Eq. (4), a nonlinear least-squares fit can be performed to estimate T_d , T_e , ϕ , and parameters describing $\hat{N}(\tilde{\nu})$ which best replicate measured values of $S_0(\tilde{\nu})$, $S_1(\tilde{\nu})$, and $S_2(\tilde{\nu})$. In this work, θ_i is known, and in a remote sensing scenario, could be determined from techniques such as LIDAR, stereo imaging, structure from motion, etc. Measurements collected from multiple viewing geometries are used to further constrain the index of refraction retrieval. This section will present a parametric model used to estimate the complex refractive index, $\hat{N}(\tilde{\nu}) = n(\tilde{\nu}) + i\kappa(\tilde{\nu})$, from P-HSI measurements.

The Lorentz oscillator model is commonly used to describe the index of refraction of materials. One drawback for remote sensing is that amorphous materials are poorly described by this model. These materials tend to have broader spectral features which vary more slowly with frequency in their refractive indices that are difficult to describe using the Lorentz oscillator model. A number of different models have been developed to describe amorphous materials, see [31–33] for some examples, and they require more parameters. Many of these have been tested in this effort but were found to be slower than the proposed method and also lacked the flexibility needed to parametrically represent $N(\tilde{\nu})$ in this work. Instead, a method was developed to solve for the imaginary component of index of refraction, $\kappa(\tilde{\nu}) = \text{Im}\{\hat{N}(\tilde{\nu})\}$, at a few equally-spaced points (or knots) and use a piecewise cubic Hermite interpolating polynomial (PCHIP as implemented in MATLAB [34]) to determine $\kappa(\tilde{\nu})$ between these knot points. This has the advantage of imposing the continuity and smoothness expected in the spectral variation of material's refractive index. Then, Kramers-Kronig relationship is used to infer $n(\tilde{\nu}) = \text{Re}\{\hat{N}(\tilde{\nu})\}$ from $\kappa(\tilde{\nu})$.

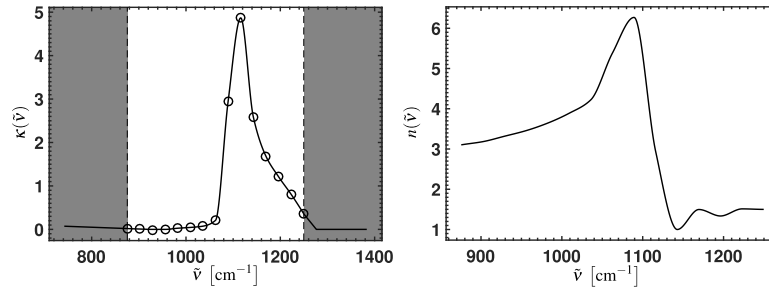


Fig. 2. *Left panel*: PCHIP interpolation (—) of the imaginary component of the refractive index, $\kappa(\tilde{\nu}) = \text{Im}\{\hat{N}(\tilde{\nu})\}$, using 15 equally-spaced knot points (\circ). Linear extrapolation, constrained such that $\kappa(\tilde{\nu}) \geq 0$, is used in the out-of-band regions shown in gray. *Right panel*: The corresponding real component of the refractive index, $n(\tilde{\nu}) = \text{Re}\{\hat{N}(\tilde{\nu})\}$, obtained from $\kappa(\tilde{\nu})$ via the Kramers-Kronig relationship.

In principle, the Kramers-Kronig relationship requires knowledge of $\kappa(\tilde{\nu})$ across all frequencies. Because only a limited spectral region is being measured, some out-of-band extrapolation of $\kappa(\tilde{\nu})$ is required. Fortunately, features in the imaginary component far from the measurement bandpass have only a small effect on the in-band behavior of $n(\tilde{\nu})$, so assuming $\kappa(\tilde{\nu}) = 0$ far out-of-band was found to be a reasonable approximation. Forcing $\kappa(\tilde{\nu}) = 0$ everywhere out-of-band, however, can introduce significant errors near the band edge. To mitigate this, linear extrapolation is used to extend $\kappa(\tilde{\nu})$ beyond the instrument bandpass to a point which is one-third of the instrument bandwidth on either end of the spectrum. Furthermore, $\kappa(\tilde{\nu})$ is set to zero anywhere that extrapolation would have led to a negative value. While more sophisticated out-of-band extrapolation schemes [35] may be required more generally, this simple method was found to work well for the materials and instrument used in this effort.

To enforce the Kramers-Kronig relationship and derive $n(\tilde{\nu})$, the imaginary component of the Hilbert transform is used:

$$n(\tilde{\nu}) = -\text{Im}\left\{\frac{1}{\pi} \int_{-\infty}^{\infty} \frac{\kappa(\tilde{\nu}')}{\tilde{\nu} - \tilde{\nu}'} d\tilde{\nu}'\right\} + n_{\infty}. \quad (5)$$

Here, n_{∞} is a model parameter representing the behavior of $n(\tilde{\nu})$ as $\tilde{\nu} \rightarrow \infty$. Using this, the Stokes vector in Eq. (4) can be described in terms of variables n_{∞} , T_d , T_e , ϕ , and κ , the vector of κ values at each knot point. For this work, 15 equally-spaced knot points were used, bringing the total number of model parameters to 19, which is more than an order of magnitude smaller than the number of independent spectral channels in the P-HSI measurements presented in this work. Figure 2 illustrates 15 knot points κ , the PCHIP-interpolated $\kappa(\tilde{\nu})$ curve, and the corresponding $n(\tilde{\nu})$ curve derived from Eq. (5).

Because the plane of reflectance can be ambiguous when the material is not solely illuminated by a point source, it is desirable to remove the ϕ term from the equations used in fitting. This can be done by creating one quantity, P , describing the total polarization,

$$P^2(\tilde{\nu}) = S_1^2(\tilde{\nu}) + S_2^2(\tilde{\nu}). \quad (6)$$

This quantity is similar to DoLP, but does not use S_0 to normalize the value. Substituting the expressions for S_1 and S_2 from Eq. (4) into Eq. (6) gives

$$P(\tilde{\nu}) = \frac{1}{2} \left(\rho_p(\tilde{\nu}) - \rho_s(\tilde{\nu}) \right) \cdot (B(T_d) - B(T_e)). \quad (7)$$

$(\rho_p(\tilde{\nu}) - \rho_s(\tilde{\nu}))$ is negative for all combination of refractive indices and viewing angles. This means that the sign of P is determined by whether the signature is reflection- or emission-dominated. Applying the correct sign to the measured total polarization, P_o given by Eq. (6), is crucial and will be exploited further later in this paper. This is done by applying the sign of either S_1 or S_2 , whichever has the larger magnitude, to P_o .

Using this and the expression for S_0 from Eq. (4), an error metric based on the observed (o) and modeled (m) quantities for both S_0 and P can be developed:

$$E(\mathbf{x}) = \sum_i \sum_j \left[S_{0,o}(\theta_i, \tilde{\nu}_j) - S_{0,m}(\theta_i, \mathbf{x}) \right]^2 + \sum_i \sum_j \left[P_o(\theta_i, \tilde{\nu}_j) - P_m(\theta_i, \mathbf{x}) \right]^2. \quad (8)$$

Here, \mathbf{x} is a vector of the fit parameters where $\mathbf{x} = [\kappa \ n_\infty \ T_d \ T_e]$. The initial fit values are $\kappa_i = 1$ for all knots points $i \in \{1 \dots 15\}$ and $n_\infty = 1.5$.

It is also important to have a reasonable starting estimate for the downwelling and surface temperatures, T_d and T_e , respectively. Eqs. (4) and (7) can be exploited to automatically determine temperature limits from the data. First, the Fresnel equations, Eq. (1) dictate that $\rho_s \geq \rho_p \ \forall n \geq 0, \kappa \geq 0$, and all θ . Thus, if P is negative, $T_d > T_e$ and vice-versa. From here, it can be determined that when $T_d > T_e$, S_0 must be greater than a blackbody at T_e and less than a blackbody at T_d . The lowest spectral brightness temperature of S_0 defines the upper limit for T_e and the highest spectral brightness temperature defines the lower limit for T_d . Likewise, in the case where $T_e > T_d$, a lower limit for T_e and upper limit for T_d can be defined. The other temperature limits are defined as 50 K greater than a lower bound, or less than an upper bound. The temperature limits can also be manually defined. The initial estimates for T_d and T_e are set to the midpoint of the established temperature bounds.

4. Instrumentation

Data was collected using a Telops long-wave infrared Hyper-Cam imaging Fourier-transform spectrometer (IFTS) with a linear polarizer mounted directly in front of and over-filling the entrance aperture. Spectral resolution $\delta\tilde{\nu}$ can be adjusted between $0.25 \text{ cm}^{-1} \leq \delta\tilde{\nu} \leq 150 \text{ cm}^{-1}$. The camera uses a 320×256 Mercury-Cadmium-Telluride (MCT) focal plane array (FPA), with spectral responsivity between $875 \text{ cm}^{-1} \leq \tilde{\nu} \leq 1250 \text{ cm}^{-1}$. Radiometric calibration is performed using two on-board blackbodies set to different temperatures chosen to bracket the scene radiance. The blackbody sources are in front of the polarizer module so that the throughput and spectral response of wire grid is accounted for during calibration. Additional information about the sensor can be found in the [36].

Polarimetric information is collected by measuring a scene through the linear polarizer at various angles. For this work, the modified Pickering method [26] is used for data collection so the scene is measured with the polarizer set to $\alpha \in \{0^\circ, 90^\circ, 45^\circ, 135^\circ\}$. The measured Stokes parameters can then be calculated: $S_0 = \frac{1}{2} (L_0 + L_{90} + L_{45} + L_{135})$, $S_1 = L_0 - L_{90}$, and $S_2 = L_{45} - L_{135}$. The Hyper-Cam polarizer has a peak extinction ratio of 350:1 and is thus nearly ideal. Holder [36] demonstrated that a two-point radiometric calibration at each angle α , as outlined in [37], is sufficient to compensate for the polarimetric response of the instrument if the polarizer is ideal. However, small non-ideal behavior can lead to systematic errors not accounted for in the model, and an effort to characterize polarimetric effects of this instrument is underway.

5. Results

Two different experiments were performed to test the index of refraction retrieval methodology previously described. The first experiment featured blackbody illumination of a quartz block to assess $\hat{N}(\tilde{\nu})$ retrieval when scattered light dominated the measured spectro-polarimetric radiance. The second experiment was performed using a Pyrex beaker on a hot plate to test retrieving

$\hat{N}(\tilde{\nu})$ when emitted light was the primary signature. Both experiments presented demonstrate the feasibility of refractive index estimation using P-HSI.

5.1. Blackbody illumination of a quartz block

A wide-area blackbody set at 115 °C was reflected off of a quartz glass (fused silica) block window, at angles $\theta_i \in \{20^\circ, 40^\circ, 60^\circ\}$ relative to the surface normal. The blackbody source allows for careful control of the downwelling radiance. Figure 3 compares measured values of $S_0(\tilde{\nu})$ and $P(\tilde{\nu})$ at each θ_i with their expected values based on the measured object temperature, blackbody downwelling radiance, and the quartz block's refractive index derived from ellipsometry. Residual differences are also provided for both S_0 and P in a panel below each comparison of measured and expected values.

The root-mean-square (RMS) of the residual differences between measured and fitted values at $\theta_i = 20^\circ$ are 0.211 ru for S_0 and 0.081 ru for P , where ru denotes radiometric units given by $\text{ru} = \mu\text{W}/(\text{cm}^2 \cdot \text{sr} \cdot \text{cm}^{-1})$. At $\theta_i = 40^\circ$, the RMS error increases to 0.240 ru and 0.104 ru for S_0 and P , respectively. At $\theta_i = 60^\circ$, the RMS error decreases to 0.197 ru for S_0 , but increases to 0.230 ru for P . The residuals do exhibit some structure and are not zero-mean, indicating some systematic biasing of the measured values.

There are a few potential sources of systematic errors. First, to the extent that the wire-grid polarizer is non-ideal, polarimetric responsivity of the P-HSI system affects the measured data, and this effect has not been characterized and removed as discussed in the previous section. Second, since the P-HSI system collects polarimetric information using a division-of-time scheme, systematic errors can be introduced by changes in scene radiance during data collection at the various polarizer angles α .

Despite several sources of systematic error, retrievals of $\hat{N}(\tilde{\nu})$ are fairly accurate. Figure 4 compares $n(\tilde{\nu})$ and $\kappa(\tilde{\nu})$ retrieved via model fitting with “truth” values derived from ellipsometry measurements. The blue curve represents the average retrieved value, and the translucent blue band about the curve represents plus/minus one standard deviation across all pixels. The green line reproduces the ellipsometry measurements. The RMS difference between the retrieved and “truth” is 0.072 for $n(\tilde{\nu})$ and 0.063 for $\kappa(\tilde{\nu})$. The average standard deviations for $n(\tilde{\nu})$ and $\kappa(\tilde{\nu})$ are 0.055 and 0.065, respectively. Note that, with only a couple exceptions, the results from ellipsometry and values retrieved from P-HSI measurements agree within the statistical uncertainty (1σ error bounds). Additionally, the places where the fit is most self-consistent (*i.e.* has the smallest error bounds) is also where it is most accurate (*i.e.* $\tilde{\nu} > 1135 \text{ cm}^{-1}$).

To assess the importance of simultaneously using $S_0(\tilde{\nu})$ and $P(\tilde{\nu})$ to estimate $\hat{N}(\tilde{\nu})$, index fitting was also performed using only one of $S_0(\tilde{\nu})$ or $P(\tilde{\nu})$. Figure 5 compares retrieved $n(\tilde{\nu})$ and $\kappa(\tilde{\nu})$ curves with ellipsometry-derived values when fitting only to $S_0(\tilde{\nu})$ (left) or $P(\tilde{\nu})$ (right). As can be seen when comparing to the results in Fig. 4, the results are degraded when only $S_0(\tilde{\nu})$ or $P(\tilde{\nu})$ is used. When used together, the hyperspectral and polarimetric components serve to constrain the fit and enable better estimates for $n(\tilde{\nu})$ and $\kappa(\tilde{\nu})$. Quantitatively, the RMS error in $n(\tilde{\nu})$ using both $S_0(\tilde{\nu})$ and $P(\tilde{\nu})$ is 0.072, compared to 0.201 using only $S_0(\tilde{\nu})$ and 0.305 using only $P(\tilde{\nu})$. Similarly, RMS errors of 0.063 are observed in $\kappa(\tilde{\nu})$ when using both $S_0(\tilde{\nu})$ and $P(\tilde{\nu})$, and increase to 0.338 and 0.272 when using only $S_0(\tilde{\nu})$ or $P(\tilde{\nu})$, respectively. Moreover, the pixel-to-pixel fit results are more consistent when using both pieces of information. The average standard deviation values, represented by the error bars in the plot, for the $n(\tilde{\nu})$ is 0.055 using both, 0.135 using only S_0 , and 0.190 using only P . Again, similar behavior is seen in for $\kappa(\tilde{\nu})$ with averages of 0.065, 0.149, and 0.200, respectively.

It is important to consider how these results will scale as the spectral features in both S_0 and P become more muted relative to the noise level of the instrument and P becomes small relative to the noise of the instrument. To explore the impact of reduced thermal contrast on index retrieval, a few simulated datasets were created using the ellipsometry-determined index of refraction

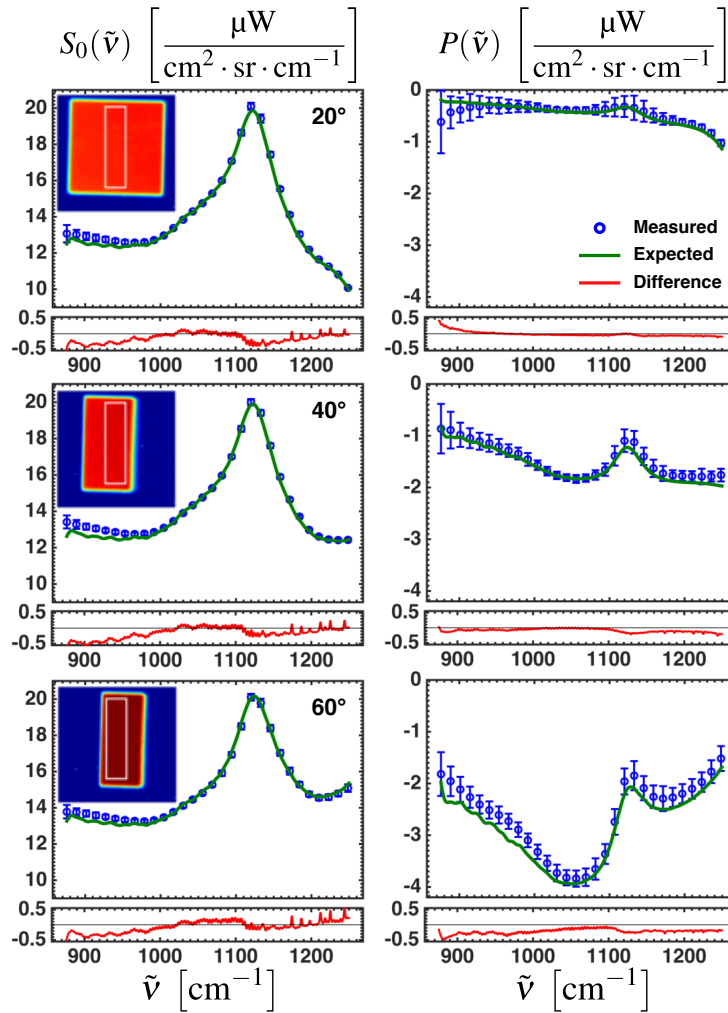


Fig. 3. *Top panel:* Comparison of measured (\circ) and expected ($—$) $S_0(\tilde{\nu})$ (left) and $P(\tilde{\nu})$ (right) values for $\theta_i = 20^\circ$. Expected values are obtained by forward modeling ellipsometer measurements of index of refraction and known object and downwelling temperatures. For clarity, only every 20 measured spectral points are shown. Uncertainties for $S_0(\tilde{\nu})$ and $P(\tilde{\nu})$ represent plus/minus one standard deviation for 500 randomly-selected pixels within the rectangle shown in the broadband image overlay. *Middle panel:* Same comparison for $\theta_i = 40^\circ$. *Bottom panel:* Same comparison for $\theta_i = 60^\circ$.

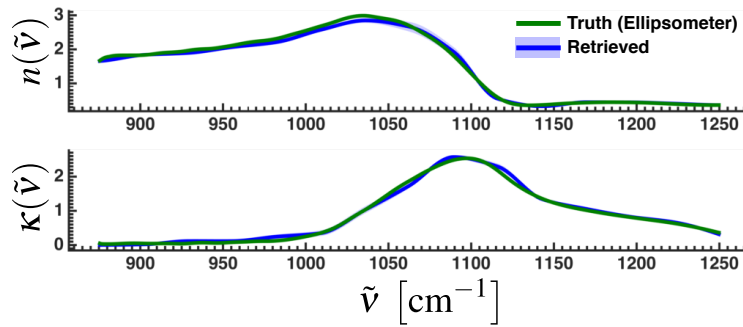


Fig. 4. *Top panel:* Comparison of fitted (—) and ellipsometry result (—) for the real part of the index, $n(\tilde{\nu})$. *Bottom panel:* Comparison of fitted (—) and ellipsometry result (—) for the imaginary part of the index, $\kappa(\tilde{\nu})$. Uncertainties for $n(\tilde{\nu})$ and $\kappa(\tilde{\nu})$ represent plus/minus one standard deviation for 500 randomly-selected pixels and are represented by the translucent blue band about the retrieved curve.

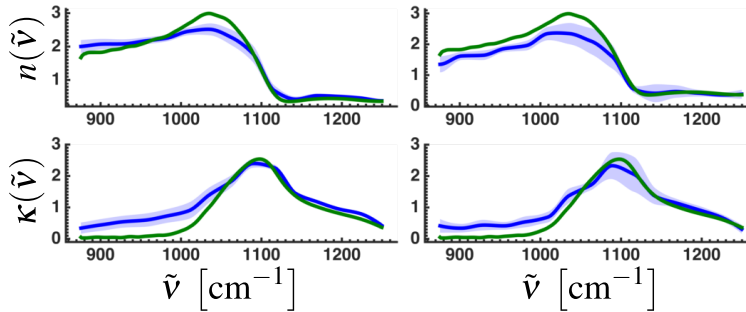


Fig. 5. Index of refraction retrieval (—) using only S_0 (left) or only total polarization P (right) compared with ellipsometry result (—). Uncertainties for $n(\tilde{\nu})$ and $\kappa(\tilde{\nu})$ represent plus/minus one standard deviation for 500 randomly-selected pixels and are represented by the translucent blue band about the retrieved curve.

for quartz and forward modeling this to S_0 , S_1 , and S_2 using Eq. (4). Normally-distributed noise representative of the instrument used for this work was added to these simulated Stokes parameters prior to retrieving the refractive index. Specifically, temperature differences between the object and background, $\Delta T = T_d - T_e$, were set to $\Delta T = 3$ K, 7 K, and 100 K, and 500 Monte Carlo simulations — one for each synthetic pixel — were performed at each ΔT . $\Delta T = 3$ K and 7 K were chosen as they represent the points where the average value of P is approximately one and two times the NESR of the instrument. $\Delta T = 100$ K was chosen as it is approximately equal to the temperature contrast of the data presented earlier.

The error in the median retrieval does not increase significantly as temperature contrast is reduced. The rms error increases from 0.0450 and 0.0629 in the real and imaginary components for the $\Delta T = 100$ K case, to 0.0723 and 0.0751 for the $\Delta T = 3$ K case. This is not unexpected as the median is taken of 500 retrievals and the noise is random. This is an indication, however, that the noise does not significantly bias the retrieval. Also, the simulated retrieval at $\Delta T = 100$ K is slightly better than the retrieval using measured data presented earlier because the simulation does not account for systematic errors, such as scene drift, which may slightly bias the data.

Of more interest is the standard deviation across the individual retrievals as this is a measure of the uncertainty in the retrieved index of refraction. As expected, the uncertainty increases as the

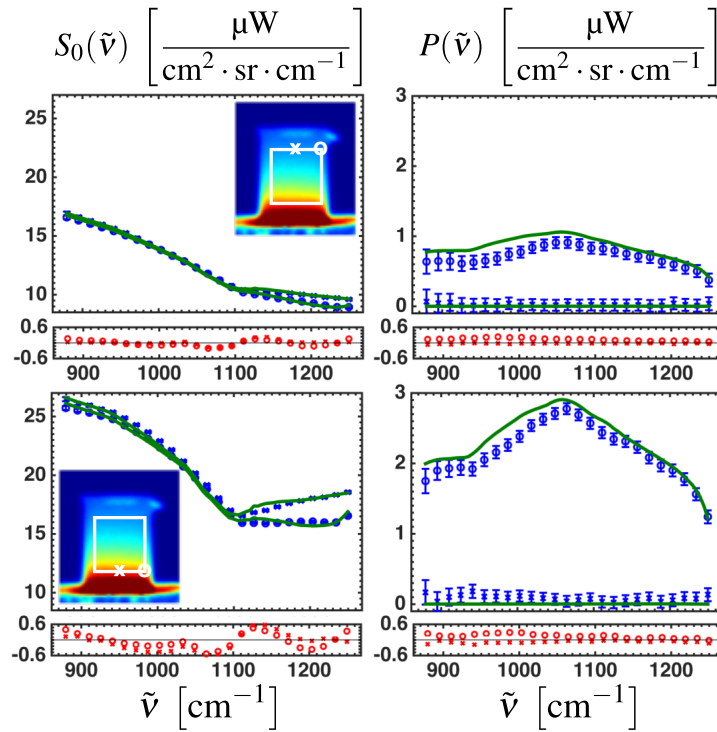


Fig. 6. *Top panel*: measured $S_0(\tilde{\nu})$ and $P(\tilde{\nu})$ values (—) compared with expected (\times , \circ) results, based on forward modeling the index of refraction and known object temperature, corresponding to $\theta_i = 0^\circ$ (\times) and $\theta_i = 55^\circ$ (\circ). Error bars represent plus/minus one NESR of the instrument as measured by Holder [36]. The red lines represent the residual between measured and expected. The white box on the superimposed images denotes the 41×40 pixel region used when fitting index of refraction. The white \times 's and \circ 's indicate the pixel locations of the corresponding $S_0(\tilde{\nu})$ and $P(\tilde{\nu})$ spectral curves.

temperature contrast is reduced. The standard deviation across all retrievals and all wavelengths for $\Delta T = 100$ K is 0.0496 and 0.0447 in the real and imaginary components respectively. When temperature contrast is reduced to 7 K, the uncertainty increases to 0.1661 and 0.1546, respectively, and at $\Delta T = 3$ K, the uncertainty is 0.3436 and 0.2875, respectively. These results, while unsurprising, illustrate the increasing difficulty in retrieving the index of refraction as thermal contrast is reduced.

5.2. Heated Pyrex beaker

A Pyrex (borosilicate glass) beaker was placed on a hot plate, generating a radiance signature that was dominated by emission as opposed to reflection. Because the heat load is at the bottom of the beaker, a temperature gradient is created with temperature decreasing up the beaker. The temperature near the bottom of the beaker was 374 K while the temperature near the top was 328 K. One of the goals of this research is to be able to robustly estimate the index of refraction regardless of object temperature. Producing a strong thermal gradient tests the index retrieval in an emission-dominated mode over a wide range of temperatures.

Since the beaker is cylindrical, the surface normal angle relative to the sensor varies from $-90^\circ \leq \theta_i \leq 90^\circ$ horizontally across the beaker. In practice, blurring by the camera's point

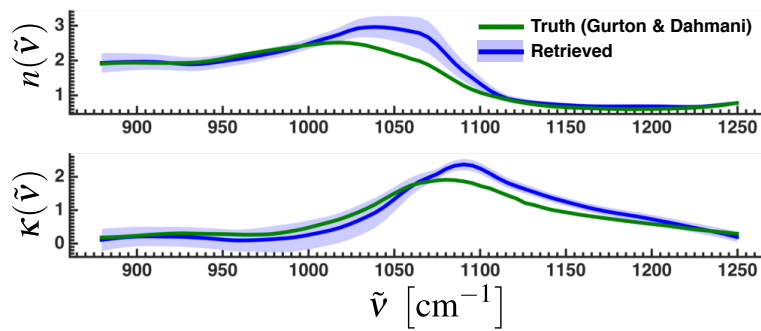


Fig. 7. Comparison of ellipsometry-determined index of refraction for Pyrex (—, Ref. [38]) with the retrieved values from the fit (—). The top and bottom panels compare $n(\tilde{\nu})$ and $\kappa(\tilde{\nu})$, respectively. The retrieved value represents an average over all 41 rows, and the shaded band represents plus/minus one standard deviation across all rows.

spread function limits the use of the outer-most pixels. In this work, the index fitting used pixels corresponding to $-55^\circ \leq \theta_i \leq 55^\circ$.

To perform the retrieval, the P-HSI imagery was cropped to a 41×40 pixel image with 41 different temperatures (*i.e.* rows of the image) and 40 different surface normal angles (*i.e.* columns of the image). Figure 6 shows the entire image of the beaker with a white box denoting the cropped region used in fitting the index of refraction. This figure also shows the measured $S_0(\tilde{\nu})$ and $P(\tilde{\nu})$, compared to the expected, again obtained via forward modeling the true index of refraction, for a normal ($\theta_i \approx 0^\circ$) and an edge pixel ($\theta_i \approx 55^\circ$) near the top and bottom of the beaker. The residuals suggest the appearance of a small systematic bias in the measured data. As expected, $P(\tilde{\nu})$ is very close to zero near the center of the beaker where the viewing angle is near-normal, and increases with both viewing angle and with increasing thermal contrast between emission and reflection (*i.e.*, near the base of the beaker where it is warmer). This figure also shows that in certain spectral regions there is a substantial change in $S_0(\tilde{\nu})$ between the middle and outside of the beaker, demonstrating the dependence of emissivity on viewing angle.

The index of refraction fitting was performed independently on each row of the image. For each row, all 40 surface normal angles are used simultaneously to estimate the refractive index. The fit results are presented in Fig. 7. These fits exhibit more error than in the quartz retrieval previously discussed. The RMS errors associated with $n(\tilde{\nu})$ and $\kappa(\tilde{\nu})$ are 0.251 and 0.207, respectively. However, unlike in the quartz experiment, ellipsometry measurements for the beaker could not be made for comparison due to its irregular shape and large size. For comparison, our “truth” values for $n(\tilde{\nu})$ and $\kappa(\tilde{\nu})$ were digitized from a graph of the index of refraction of Pyrex in a paper by Gurton *et al* [38]. It is possible that some discrepancy arises from differences in Pyrex used in this and Gurton’s work. Another source of systematic error likely arises from assuming each pixel observes a single θ_i . Due to blurring effects, each pixel observes radiance from a range of different viewing angles, particularly near the edges of the beaker. The effect of angle mixing is nonlinear, so the observed radiance will not be identical to the radiance expected from the pixel’s average viewing angle.

While the variance among individual retrievals is larger for the heated Pyrex beaker than was observed for the quartz block, it is uncorrelated with the retrieved temperature. The average coefficient of determination (r^2) between temperature and the fitted index, across all spectral bands, is 0.07 for $n(\tilde{\nu})$ and 0.02 for $\kappa(\tilde{\nu})$. This indicates that the retrieval method is robust across a wide range of temperatures.

6. Conclusions

A method for retrieving the complex index of refraction, $\hat{N}(\tilde{\nu})$, from polarimetric hyperspectral imagery (P-HSI) has been developed. A parametric model for the imaginary component featuring a piecewise cubic Hermite interpolating polynomial was used to describe the spectral variation in refractive index and enforce smoothness, and the Kramers-Kronig relations were used to determine the real component.

This effort demonstrated that the complex refractive index can be retrieved to within 0.08 RMS error for a smooth quartz window observed in a reflection-dominated mode. Additionally, emission-dominated measurements of a smooth Pyrex beaker demonstrated that object temperature and refractive index could be independently determined with minimal correlation between the two parameters.

By using a low-dimensional model to describe $\hat{N}(\tilde{\nu})$, additional physical parameters (*e.g.*, object temperature) can be included in the retrieval. This approach could find applicability in temperature-emissivity separation problems and enable more robust material identification. Future work will focus on incorporating atmospheric effects and bidirectional reflectance distribution functions for rough surfaces. This will enable assessing the performance of refractive index retrievals for more realistic targets over longer path lengths in an outdoor environment.

Acknowledgments

Thanks to the Defense Threat Reduction Agency for sponsoring this effort via grant # 2437-M.